Ground Support 2026 - D Cumming-Potvin & J Wesseloo (eds.)
© 2026 Australian Centre for Geomechanics, Perth
doi:10.36487/ACG_repo/2625_35

Monitoring to model: harnessing extensometer data to enhance the geotechnical model for better predictions

Andrew Wilson [a,*], Rudy Subur [a], Matthew Cowan [a], Daniel Barnett [b]

[a] *Tropicana Gold Mine, AngloGold Ashanti, Australia*

[b] *Operational Geotechs, Australia*

Abstract

Extensometers in their various forms are used in underground applications for the monitoring of rock displacement or deformation and to manage risk associated where large spans, narrow pillars or squeezing ground are present (to name a few). Whilst the data obtained from these instruments may primarily be most useful in giving warning prior to movement or failure, the data can also be used to identify the method in which failures occur at the site-specific scale and may well prove to be useful tools in calibrating numerical models used in geotechnical planning and design of mining shapes. In this fashion, the extensometer can and should also be viewed as a tool in the iterative process of model calibration for underground operations, rather than just as a warning device. To ensure the integrity and reliability of such an instrument when used in this way; however, the full process from instrument installation, monitoring and data collection, data interrogation, analysis, and model evaluation needs to be planned and executed correctly.

Tropicana Gold Mine (TGM) has used SMART cable data in conjunction with other underground rock failure data to calibrate its primary numerical model and determine the likely mode of failure/deformation expected mining depths where monitoring took place. This case study focuses on a scenario where SMART cable data was obtained from the backs of a 4-way intersection inside a large, multi-stage bulk stope, and although the instrument was installed primarily for risk management purposes, the data has shown its worth in numerical model calibration. Additionally, the data demonstrates the potential for this methodology to evaluate ground support performance and to assist with forecasting future ground support requirements at depth (pending further independent validation). The installation process, data interrogation and analysis steps are outlined throughout as a reference for others attempting a similar endeavour of model calibration using underground extensometers.

Keywords: *extensometer, numerical modelling, model calibration, ground support, instrumentation*

1 Introduction

1.1 Tropicana Gold Mine underground overview

Tropicana Gold Mine (TGM) is located approximately 330 km northeast of Kalgoorlie in Western Australia on the edge of the Great Victoria Desert (Figure 1). The mine commenced open pit operations in 2012 with the commencement of Havana and Tropicana open pits. Underground operations commenced in 2019 with first gold production 12 months later in 2020 in the Boston Shaker (BS3 and BS4) underground mines (Tropicana Joint Venture 2023). Currently, TGM consists of an active open pit in Havana and active underground production from the BS3, BS4 and TP3 orebodies, with development towards the Havana underground orebody well underway (Figure 2).

[*] Corresponding author. Email address: awilson@aga.gold

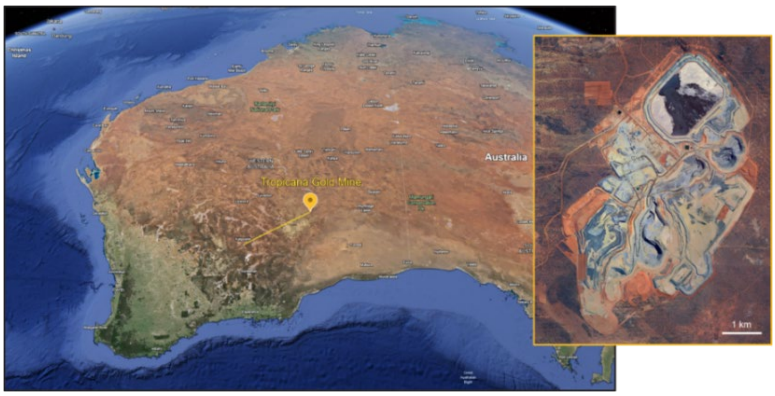


Figure 1 Tropicana Gold Mine location overview

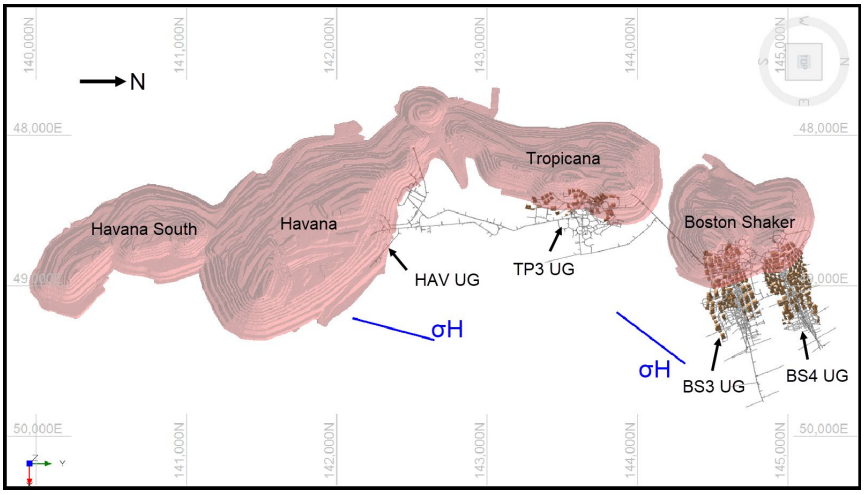


Figure 2 Tropicana Gold Mine open pit and underground mines showing regional maximum strength azimuth

Gold mineralisation at TGM is flat to intermediate-dipping, generally dipping 30 to 45°. The primary mode of gold extraction for underground operations is via the longhole open stoping (LHOS) method, with level spacings between 17–20 m. The deepest active underground development and production mining is occurring in the BS3 orebody. Production is at 580 m below surface (mbs), whilst development is at 680 mbs (Figure 3).

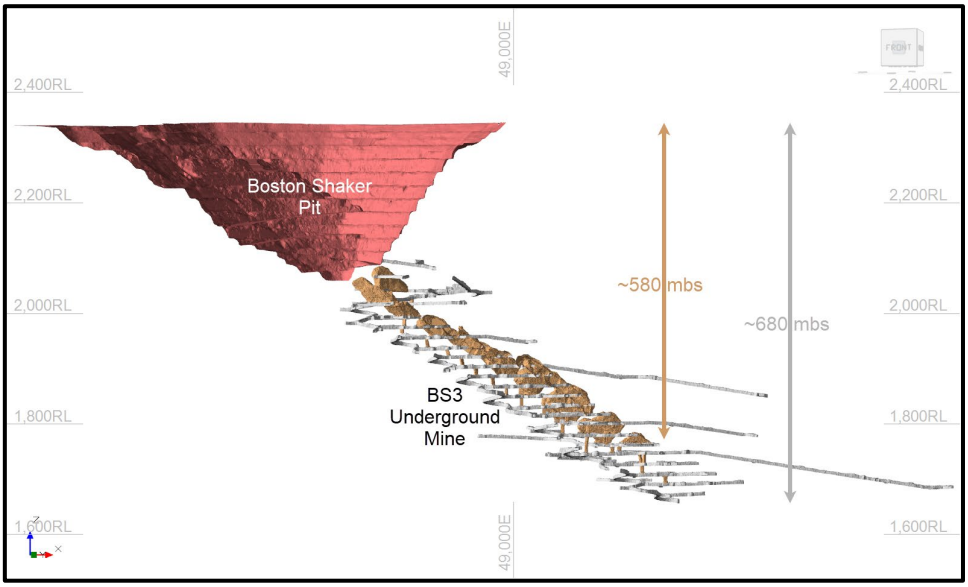


Figure 3 Section view of Boston Shaker pit and BS3 underground mine as of 2026

Gold is disseminated at TGM. As such, the economical orebody is typically 10–20 m wide (normal to the dip). However, in some locations such as the BS3 orebody, single stopes have been mined to >40 m thick and across multiple levels. This study in particular focuses on a triple-lift stope in the BS3 south, mined to dimensions ~60 × ~60 × ~28 m (height × width × strike).

The geology of orebody at TGM primarily consists of foliated Archean Feldspathic Gneiss hosting mineralisation, with garnet-bearing gneiss (ANG) constituting the footwall and hanging wall of the orebody. Both gneissic units are generally relatively high-strength, with uniaxial compressive strength (UCS) testing of core samples placing them typically 150–250 MPa. Cross-cutting regional shears typically comprise of schist (AZ), which are lower strength and rarely have a UCS greater than 100 MPa (Figure 4) (Brockman 2018).

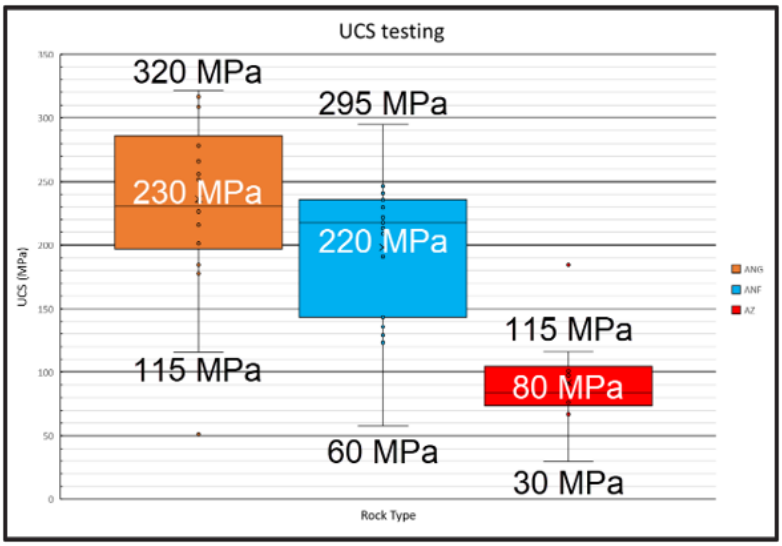


Figure 4 Uniaxial compressive strength (UCS) test results of the 3 dominant rock types at Tropicana Gold Mine

The main geotechnical considerations when designing stope shapes are pervasive gneissic foliation, which can result in bulk slabbing failure in stope hanging walls, as well as cross-cutting shear zones which can also contribute to hanging wall dilution. Data from Mills & Puller (2024) indicates the regional maximum stress, particularly in the BS3/BS4 orebodies, is shallow and orthogonal to sub-perpendicular to the orebody, concentrating in stope pillars (Figure 2). Historically, there have been a handful of cases of fretting pillars to full pillar failures at TGM (stope pillars with no personnel access) due to kinematic mechanisms or over-stressing of slender pillars. Most of these cases were by design as calibration pillar failures, in order to obtain site-specific data for designing pillars.

1.2 Current cable bolting design rationale

Cable bolt patterns at TGM are primarily designed for large development spans (for personnel access) and as hanging wall cable bolts to support stope spans.

Development cable bolts are installed in intersections and any capital infrastructure where spans are large enough that they are not adequately supported by the primary ground support pattern. An example of an intersection pattern can be seen in Figure 5.

The current hanging wall cable bolting regime for the intermediate-dipping orebody is intended to reinforce the rock mass and create stable structural beams across the extraction span. The design aims to minimise unsupported spans and reduce the likelihood of hanging wall relaxation and failure, by limiting stope spans during mining. This can be visualised in Figure 6.

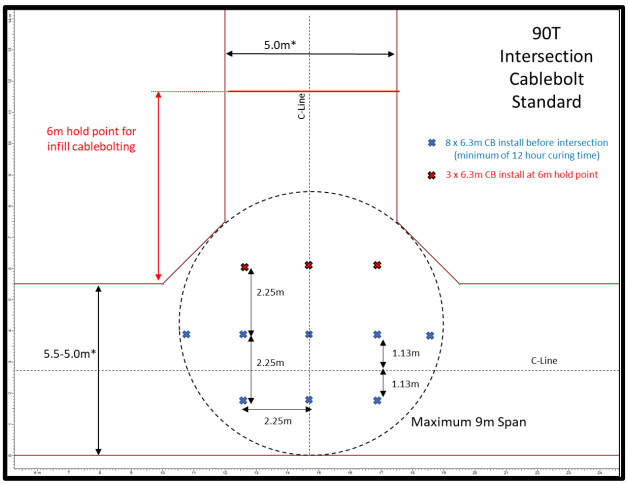


Figure 5 Example of development intersection cable bolt (CB) pattern employed at Tropicana Gold Mine (TGM Geotechnical 2026)

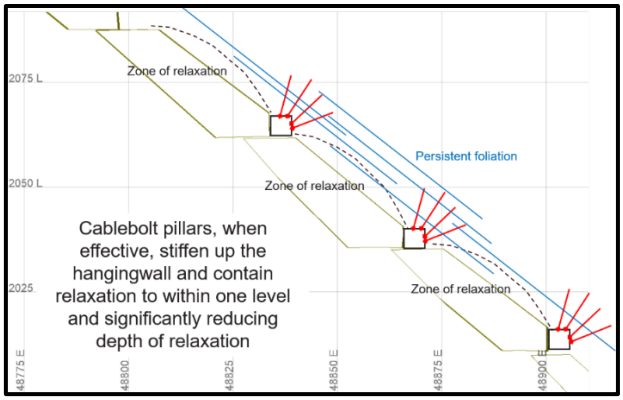


Figure 6 Example of hanging wall cable bolting rationale employed at Tropicana Gold Mine (Brockman 2018)

1.3 Instrumentation in higher-risk locations to enhance operational safety

Cable bolt-extensometers are utilised and installed in areas of concern or anticipated instability, by measuring strain, displacement, and load at various nodes along the length of the instrument when installed in a borehole and monitored regularly.

Extensometer locations that have been considered include areas susceptible to time-dependent deformation or instability, such as large spans associated with long-term capital development, narrow pillars, or access drives located near major geological structures.

At TGM, a number of extensometers have been installed in underground locations for the purpose of monitoring short and long-term ground movement or reaction to mining-induced stresses for personnel access requirements. Typically, these extensometers are installed in larger spans (i.e. development intersections) as part of the cable bolt design pattern, and monitored monthly or, in the case of nearby stoping, after every stope firing.

This case study will focus on a 6 m long cable bolt extensometer installed in a vertical borehole (TRGM-S0921-1) in the centre of an intersection cable pattern in a 4-way intersection inside a large triple-lift bulk stope at ~400 mbs, the BS3 1890 52S stope (see Figure 7) comprising 15 individual firings shapes (F1–F15). At the time of the study 4-way intersections were not frequently developed at TGM, especially not in proximity to large bulk stopes, so the behaviour of the rock mass above these intersections was largely unobserved until this point.

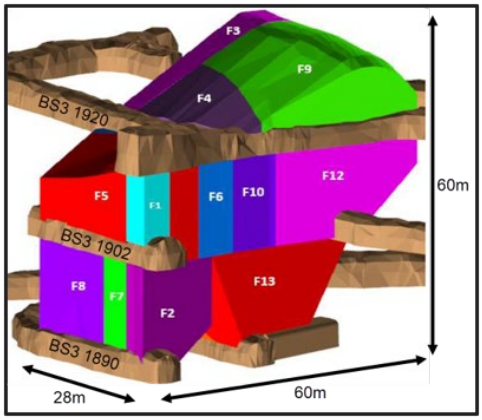
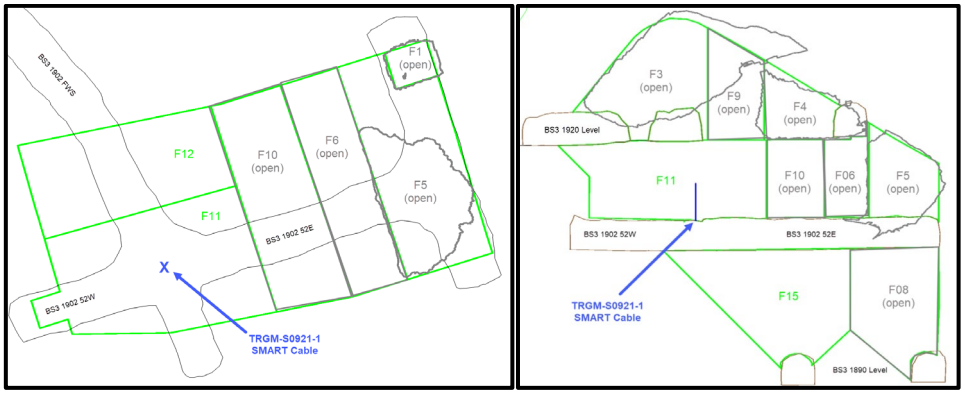


Figure 7 The BS3 1890 52S stope showing comprising firing shapes (F1-F15) (TGM Geology 2023)

The TRGM-S0921-1 extensometer contains 6 nodes (strain gauges) spaced 1 m apart along the length of the cable bolt – each node is central and contained inside cable bolt bulbs. During installation, the cable bolt was installed as per site-standard as a twin-strand cable bolt and using a modified plate with a notch cut out for the readout lead cable to safely exit the collar. To ensure adequate coupling of the bolt to the rock mass along the entire length, full grout encapsulation using 0.35 W:C ratio low-heat grout was achieved via pressure grouting. Standard measurement uncertainty is specified by the manufacturer as being ± 2% linearity, which for this instrument is ~1 mm displacement uncertainty (per node).

The primary intended function of this extensometer was to monitor the intersection span, located inside firing 11 (F11, see Figure 8), as the development and stoping sequence progressed toward it, therefore introducing potential for significant induced stresses and/or relaxation zones due to the retreating brow.



(a) (b)

Figure 8 Location of extensometer TRGM-S0921-1 inside the BS3 1890 52S stope. (a) Plan view; (b) Section view (TGM Geotechnical 2023)

2 Monitoring data results

2.1 Development and stoping sequence

This extensometer was monitored after each development and stope firing over the length of the study (3 months). Overall, there were 4 individual development firings (BS3 1902 52W slot development) and 7 subsequent individual stope firings (F1/F2 had been mined prior to installation, F8+F10 shapes taken together) before the extensometer was destroyed and intersection removed in the F11 firing.

A timeline of the sequence of events of the extensometer installation and BS3 1890 52S development and stope firings can be seen in Figure 9. Images were obtained from building a recreation scenario in numerical modelling software.

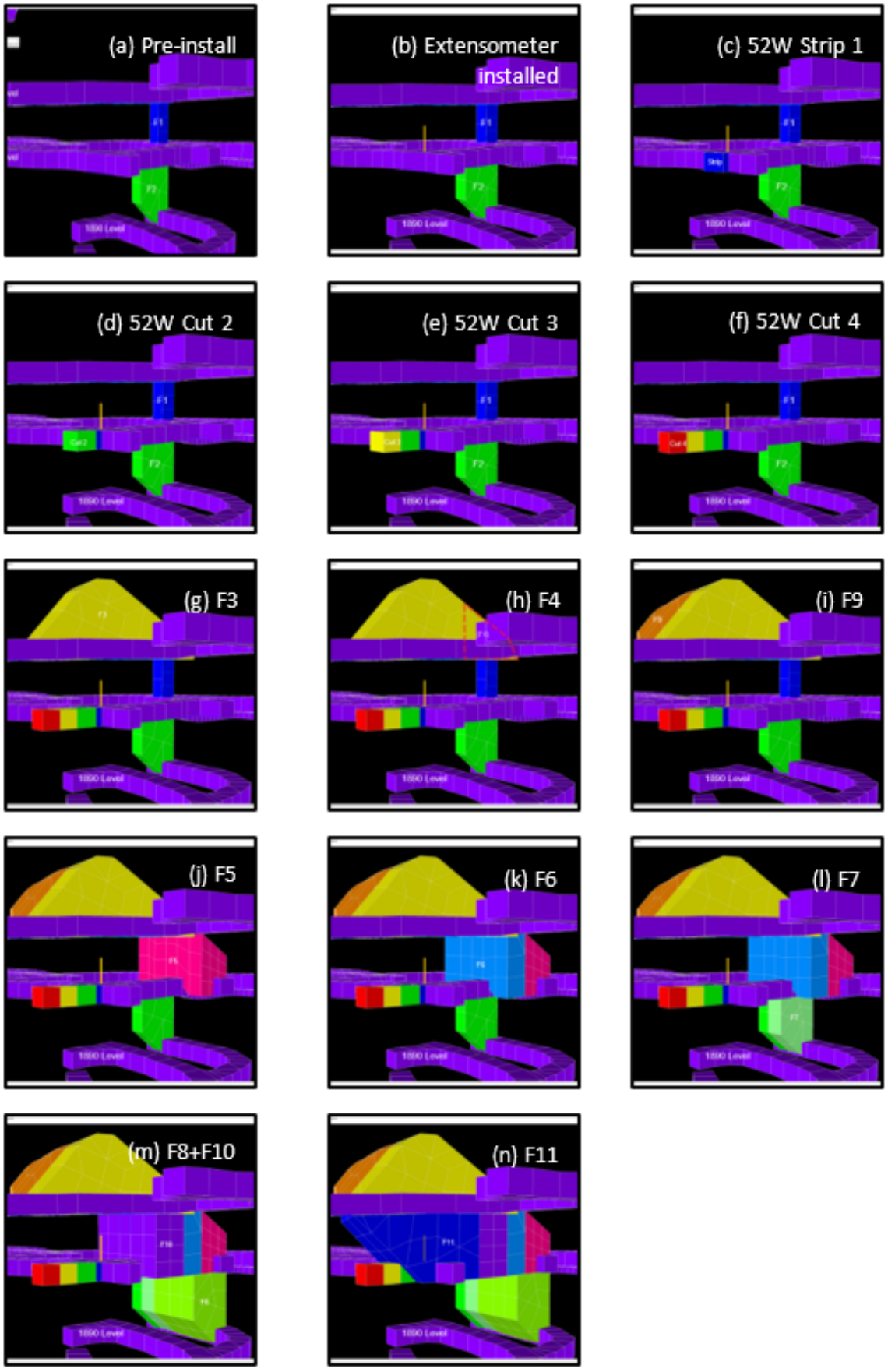


Figure 9 Sequence of events (a) through (n) showing installation of cable extensometer TRGM-S0921-1 and development and stope firings for BS3 1890 52S bulk stope

2.2 TRGM-S0921-1 extensometer displacement data

The resulting raw displacement over time data of the extensometer is seen in Figure 10, and a change in displacement over time along the length of the instrument can be visualised in Figure 11. Additionally, a summary table of the sequence of events with key findings is shown in Table 1.

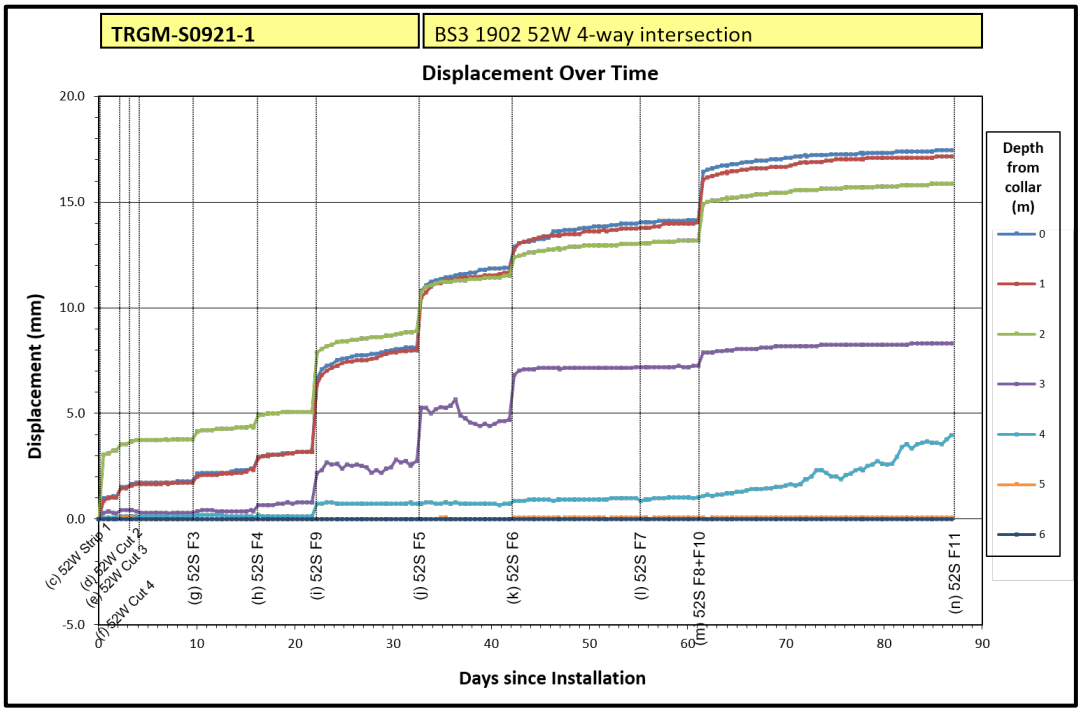


Figure 10 Displacement over time graph of extensometer TRGM-S0921-1, showing displacement of each node as well as firing event timestamps

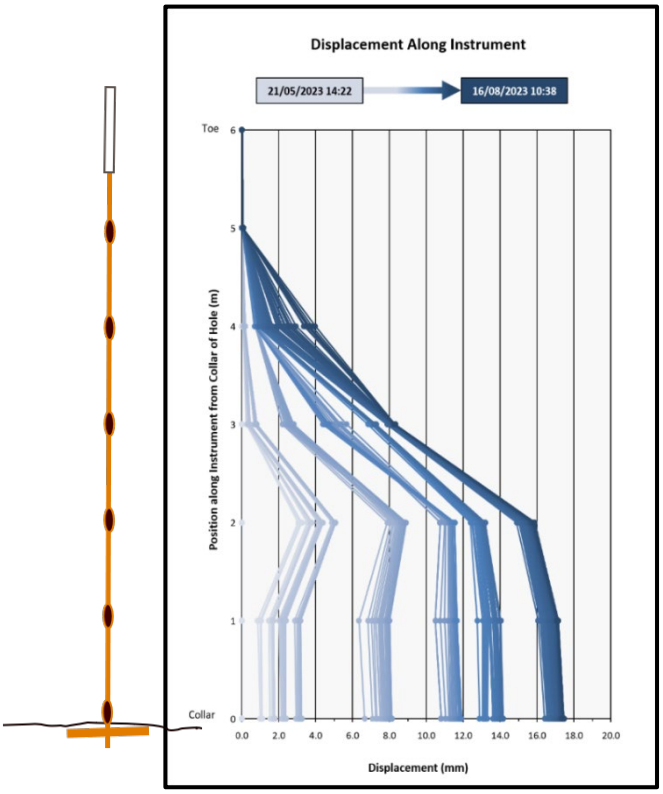


Figure 11 Change over time in displacement along the length of cable bolt extensometer TRGM-S0921-1

Table 1 Summary of key displacements observed in extensometer TRGM-S0921-1 data

Sequence frame (Figure 9)	Sequence step or firing	Days after installation	Key displacement observations
(a)	Pre-installation (F1+F2 already fired)	–	–
(b)	Installation of extensometer TRGM-S0921-1	0	–
(c)	Slot drive BS3 1902 52W Strip 1 fired	0 (same day)	~3 mm @ 2 m node
(d)	52W cut 2 fired	2	~0.5 mm @ 1 m node
(e)	52W cut 3 fired	3	Minor
(f)	52W cut 4 fired (end of development)	4	Negligible
(g)	BS3 1890 52S F3 fired	9	~0.5 mm @ 2 m node
(h)	52S F4 fired	16	~1 mm @ 2 m node ~0.5 mm @ 3 m node
(i)	52S F9 fired (out of sequence)	22	*Significant displacement event* ~5 mm @ 2 m node ~0.5 mm @ 4 m node
(i) to (j)	Between firings F9 to F5	22–32	Ongoing stress readjustment @ 3 m node
(j)	52S F5 fired	32	*Significant displacement event* ~3 mm @ 3 m node
(j) to (k)	Between firings F5 to F6	32–42	Ongoing stress readjustment @ 3 m node
(k)	52S F6 fired	42	*Significant displacement event* ~2.5 mm @ 3 m node
(l)	52S F7 fired	55	Negligible
(m)	52S F8+F10 fired (double firing)	61	~2 mm @ 2 m node ~1 mm @ 3 m node
(m) to (n)	Between firings F8+F10 and F11	61–81	Ongoing displacement creep @ 4 m node
(n)	52S F11 fired, intersection and extensometer removed	87	End of data

2.3 Displacement data conclusions

Over the study period, the cable bolt extensometer data showed clear and discrete displacement events at points along the length of the instrument, coinciding with the firing events of the BS3 1890 52S stope. By the end of the study period, the majority of displacement had occurred between 2–3 m depth above the intersection (16–17 mm), decreasing above that at 3–4 m depth (~8.5 m) and again at 4–5 m depth (~4 mm), to showing negligible displacement at 5 m depth and above. The progressive formation of tension arch displacement and depth within the intersection highlights the multiple loading conditions intersection support may endure during its life cycle, particularly when in proximity to stoping abutments and/or stress shadowing.

Ongoing instability between 3–4 m depth between F9 and F6 firings (days 22 to 42) may indicate the ground reacting to significant induced stresses concentrating through the pillar above the intersection due to the large proximal stope firings. The displacement creep observed at 4 m depth, from F8+F10 onwards, likely indicates relaxation in the rock mass at that depth caused by the unconfinement of the nearby stope brow to the intersection.

3 Monitoring to model: using extensometer data to calibrate the Tropicana Gold Mine numerical model

3.1 Numerical model overview

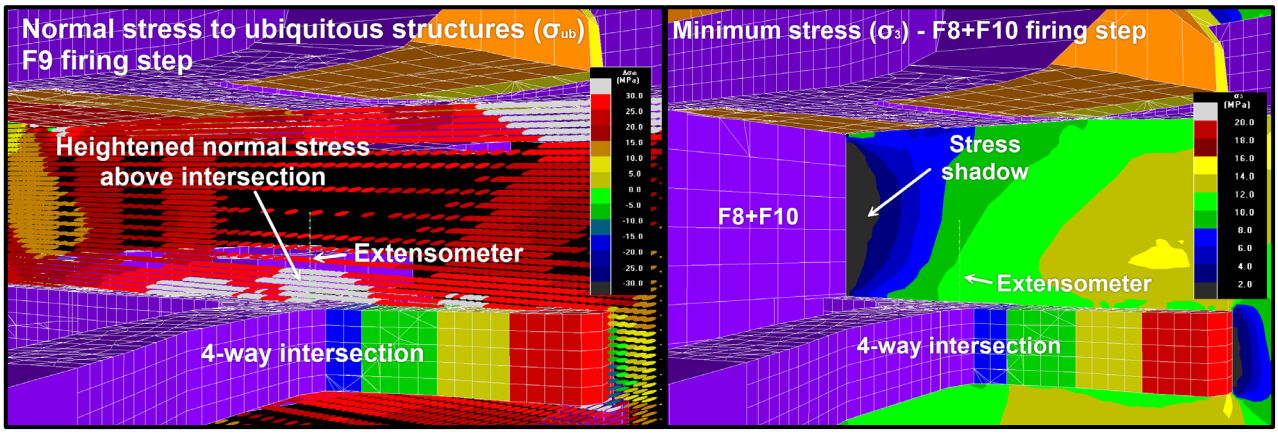
Numerical modelling was conducted using Map3D, and to accurately capture the induced stresses of the BS3 1890 52S stope sequence, a refined mesh density of 1 m was applied to the intersection in vicinity to the extensometer. The model was also built with existing development and stope voids sufficiently far from the area of interest.

The rock mass parameters of the numerical model were based on data obtained from laboratory strength testing. For the dominant gneissic rock mass, this included a Young's modulus of 70 GPa, Poisson's ratio of 0.3, and Mohr–Coulomb parameters of 30° friction angle and 17.3 MPa cohesion, which were also used for the ubiquitous structural planes.

By recreating the sequence of events in the TGM numerical model with known stress regime (measured), the stress state of key displacement events can be observed. Included in the numerical model are ubiquitous structural planes, pervasive main structures mapped at TGM and with measured structural properties including friction angle (ϕ) and cohesion (Coh).

Some examples of phenomena in the (uncalibrated) model can be seen in Figure 12. These include a parabolic arch of heightened stress formed at the location of the extensometer above the 4-way intersection with progressive firings, as well as an approaching stress shadow above the intersection with the encroaching stope brow, by this stage the parabolic arch has been lost.

The numerical model highlights the complex combination of failure modes experienced by the extensometer throughout the progression of firings, and the strong influence of the stope brow on the stress regime above the intersection.



(a) (b)

Figure 12 (a) Heightened normal stresses exerted on ubiquitous structural planes (σ_{ub}) at the extensometer location after F9 firing; (b) Low minimum stress (σ_3) shadow encroaching above extensometer location due to nearby brow after F8+F10 firing

3.2 Determining rock mass versus structure-oriented failure relationships

There is now a small population of spatial and temporal data obtained from the TRGM-S0921-1 extensometer readout, which can be interrogated against the numerical model to attempt to determine a better-fitting failure criterion of the rock mass, and therefore calibrate the numerical model to better estimate the extent of ground movement (or even overbreak). The methodology of calibration in this paper can be seen in, and was inspired by, the methodology employed by Wiles (2007).

The 2 failure criterion that can be analysed are rock mass failure – where the rock mass itself fails due to the maximum stress (σ_1) exceeding a given minimum stress (σ_3) (Equation 1) – and structure-oriented failure – where ground failure occurs along structural planes whereby the shear stress (τ) exerted on structures exceeds their corresponding normal (clamping) stress (σ) (Equation 2):

$$\sigma_1 = UCS + q \times \sigma_3 \quad (1)$$

where:

UCS = the intercept of the best-fit line

q = slope of the best-fit line.

$$\tau = \mathrm{Coh} + \tan(\varphi) \times \sigma \quad (2)$$

where:

Coh = the intercept of the best-fit line

$\tan(\varphi)$ = slope of the best-fit line.

To do this, each development and stope firing was numerically modelled using the TGM stress model parameters. The extensometer data provides discrete displacement depths at different stages in the sequence, and so each step of the model can be interrogated to obtain the boundary between displaced and non-displaced rock mass above the intersection, through changing stresses over time, see Figure 13. It should be noted that this process represents the calibration of these displacement indicators, not the full validation of the entire numerical model.

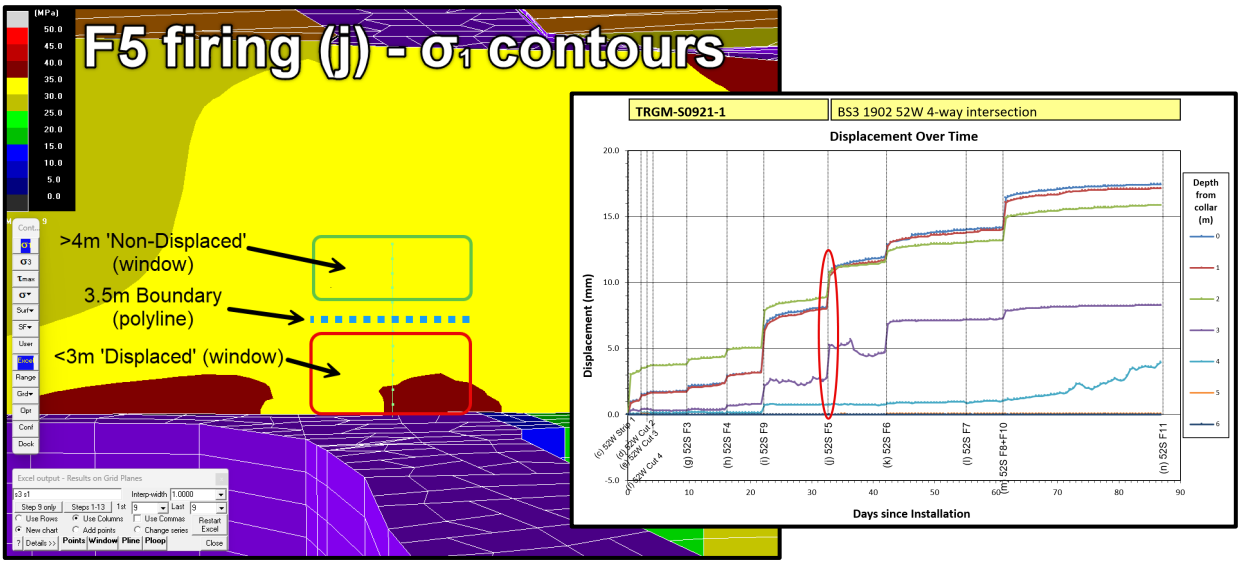
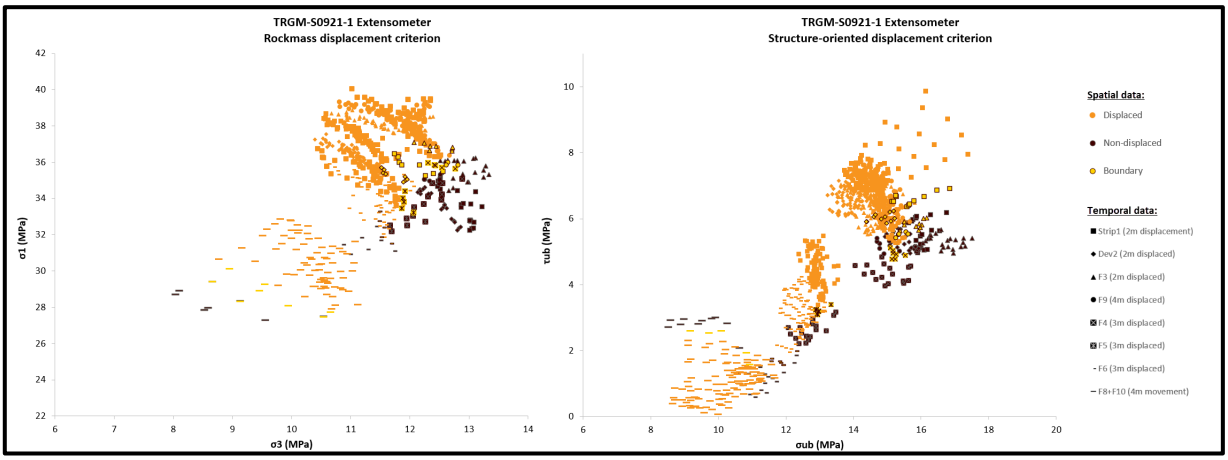


Figure 13 Plotting σ_1 versus σ_3 at measured depth of displacement (F5 example)

To generate the regression dataset for this analysis, stress tensors (σ_1, σ_3, normal stress σ_{ub}, shear stress τ_{ub}) were extracted from the numerical model at each extensometer node position, for each firing step. Displaced bins were taken as the depths of each node exhibiting displacement from the extensometer data (>1 mm),

and non-displaced bins from nodes not exhibiting displacement (<1 mm). Boundary points were also taken at 0.5 m (halfway) between the displaced and non-displaced node depths.

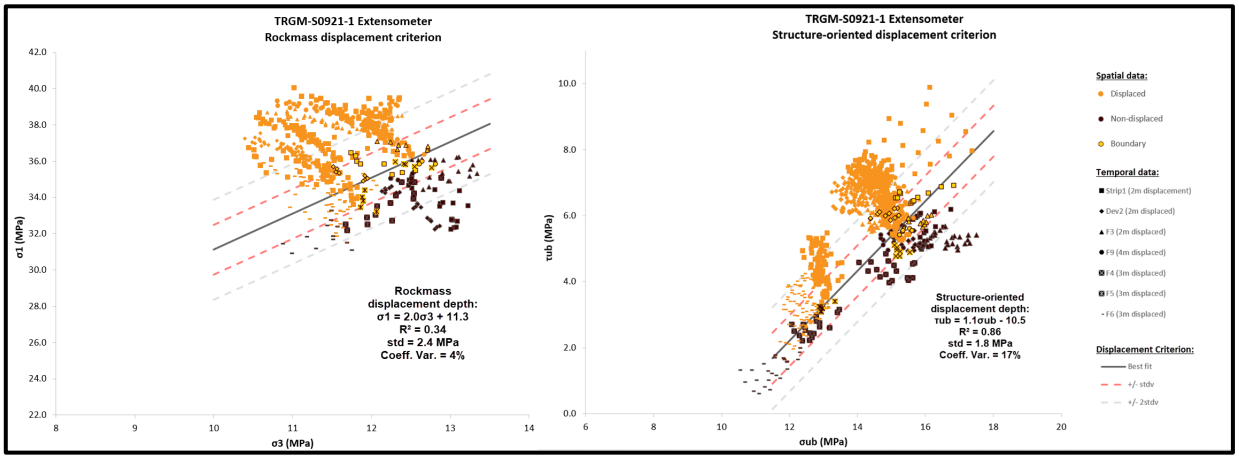
The output plots for both rock mass displacement and structure-oriented displacement can be seen in Figure 14, which distinguishes both spatially (displaced/non-displaced/boundary) and temporally (firing event). General trends can be observed in these plots where displaced points are separated by non-displaced points, with boundary points trending approximately in-between. However, of interest to note are the outlying F8+F10 firing results clusters, which may be indicative that the failure mode of the rock mass is no longer a Mohr–Coulomb relationship but rather due to relaxation in the rock mass due to the encroaching brow. Alternatively, another possible explanation for the F8+F10 results is that the failure mode still follows a Mohr–Coulomb curve, but that 'the curve itself' may have changed, as the material characteristics of the rock mass may have changed over time, being subject to numerous proximal blasts.



(a) (b)

Figure 14 Output plot of (a) σ_1 versus σ_3 (rock mass displacement) and (b) τ_{ub} versus σ_{ub} (structure-oriented displacement) for main observed displacement events

Removing the F8+F10 outliers, a better relationship is observed for both plots. The best-fit of the boundary between displaced and non-displaced data was determined, along with a normal distribution envelope (±2stdv) which can be seen in Figure 15. Coefficients for criteria Equations 1 and 2 have been achieved.



(a) (b)

Figure 15 (a) Rock mass displacement and (b) structure-oriented displacement relationships determined

4 Discussion of results

The relationships observed indicate that, between the displacement criteria, the structure-oriented displacement holds a better behavioural trend over the rock mass displacement relationship (R^2 of 0.86 versus 0.34) and therefore may be more suited for the purpose of predictive modelling. Omitted so far from this paper is the fact that, historically, displacements and stope overbreaks at TGM are typically structurally controlled rather than failure of the rock mass itself, this knowledge bias is removed for the purpose of this discussion.

The structure-oriented criterion yielded a relationship $\tau_{ub} = 1.1\sigma_{ub} - 10.5$, which (as per Equation 2) equates to a friction angle of ~47.7°, and a resulting negative cohesion intercept of -10.5 MPa. This negative cohesion may appear physically counterintuitive; however, it is a mathematical artefact of applying a linear regression to a failure envelope that is non-linear at low-confining stresses. By solving for the stress shadow threshold (τ =0), a normal stress of σ = 9.5MPa is achieved. Therefore, this may signify that once the normal stress acting on structural planes drops below 9.5MPa, there is a complete loss of interlocking between the rock mass structures (which aligns with the loss of confinement when the F8+F10 stope brow encroached on the intersection).

Importantly, it can be said that the data contains an exceptionally high amount of information given the fact that it has been sourced from a single instrument, but it is for this reason that the dataset is also very confined. Data from more locations is required to produce a more reliable calibration and to enable true validation of the larger numerical model. Ideally, this would include extensometer data from more locations around the mine for consistency, but another dataset could potentially be found in stope overbreak from reliable stope scanning data.

Nevertheless, the results achieved can be checked in the numerical model by replacing the rock mass and structural parameters of the uncalibrated model with those from the relationships. Strength factor (SF) comparisons between uncalibrated and +1stdv relationships, for both criteria, have been shown in Figure 16 (F9 firing, sequence frame *i*) and Figure 17 (F8+F10 firing, sequence frame *m*).

As can be seen for all results, the uncalibrated model fails entirely to predict the displacement measured by the extensometer, showing a minimum SF of 1.8 for all models. It also fails to predict stope hanging wall overbreak potential.

When the criteria are applied to the F9 firing, both relationships show the parabolic tensile arch above the intersection and are able to approximate the depth of displacement (SF < 1.0) observed by the extensometer in this firing, with the rock mass criterion having a slight edge in predicting the true depth of displacement. Both models also show stope hanging wall overbreak potential; however, the rock mass criterion does a better job of defining the SF = 1.0 boundary.

For the F8+F10 firing, assuming the intersection is experiencing full relaxation from the nearby stope brow and no longer following a Mohr–Coulomb failure mode, the structure-oriented criterion does a much better job of predicting the true depth of displacement, whilst the rock mass model indicates no displacement above the intersection (SF ~1.2). Regarding hanging wall conditions, both criteria show overbreak potential for this firing, but structure-oriented criterion fails to define a SF = 1.0 boundary.

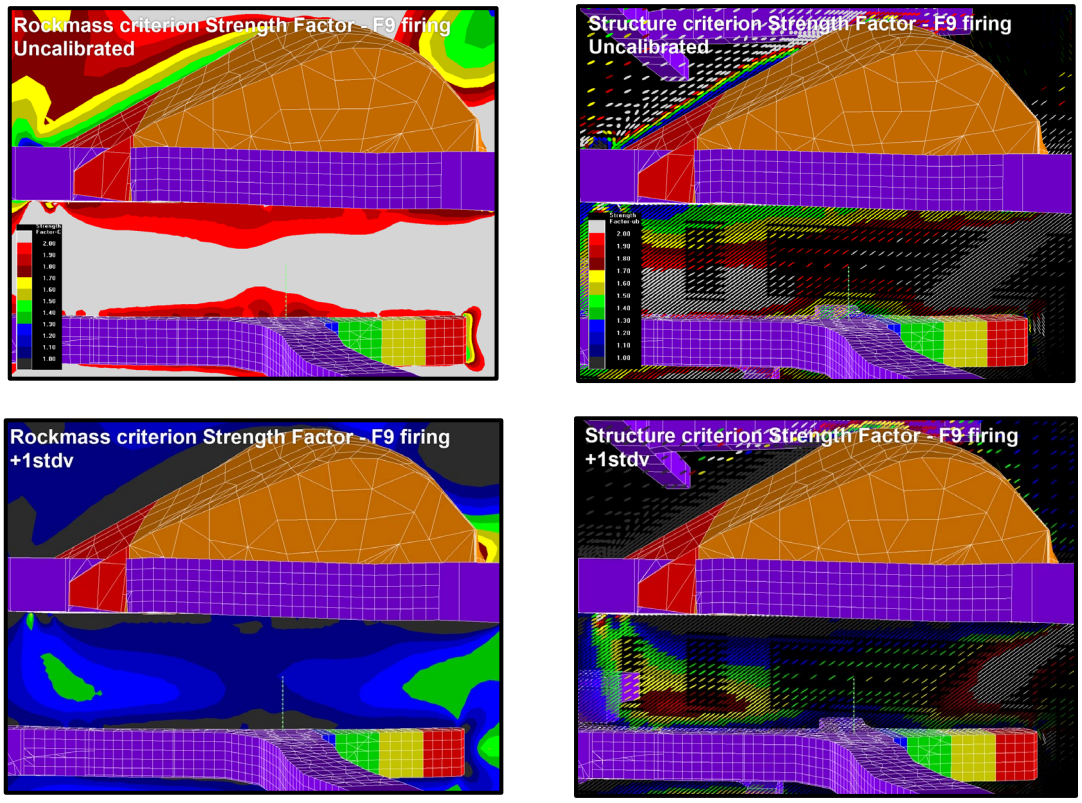


Figure 16 Post-F9 firing strength factor for rock mass and structure-oriented displacement criteria, comparing the uncalibrated model to the achieved +1std relationship model

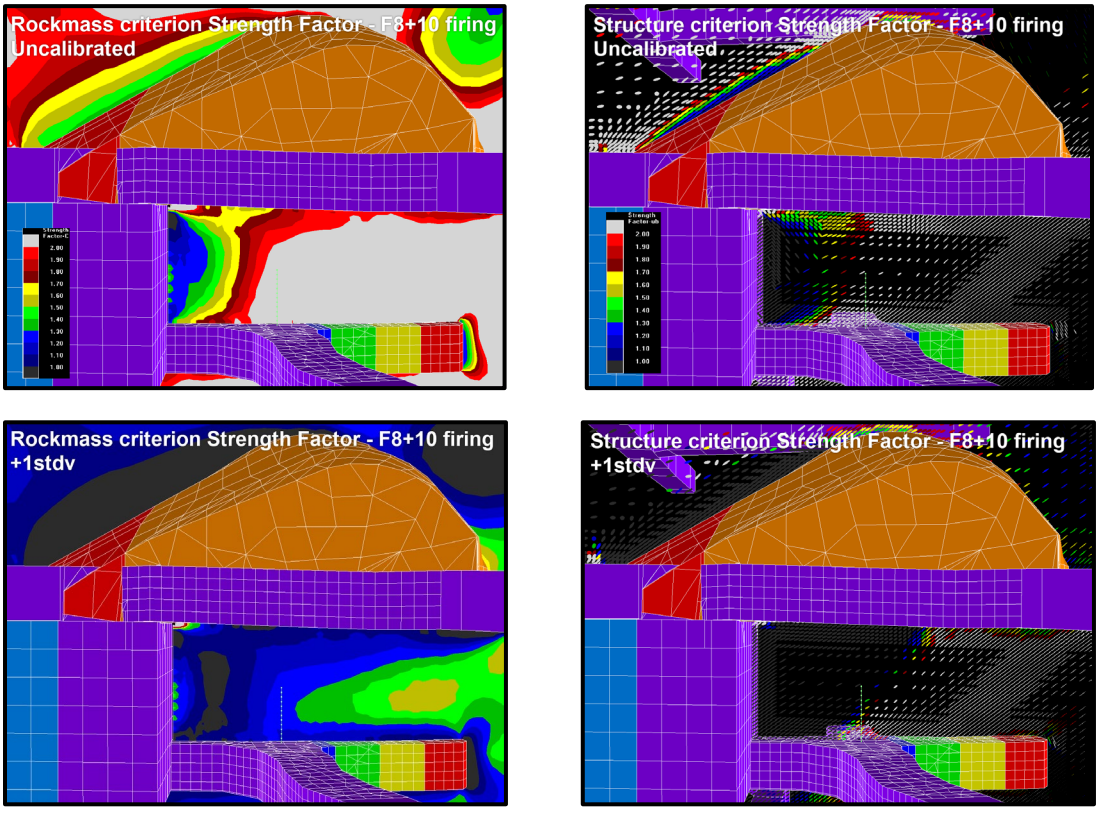


Figure 17 Post-F8+F10 firing strength factor for rock mass and structure-oriented displacement criteria, comparing the uncalibrated model to the achieved +1std relationship model

5 Conclusion

In conclusion, this study provides a strong foundation for approximating or predicting depth of displacement in higher-risk intersection locations at TGM. The fact that both parabolic tensile arch and brow relaxation modes of ground displacement could be approximated by the structure-failure criterion indicates it is the more likely failure mode at TGM for this specific scenario. As stated above, this is a single time-dependent dataset, and in order to validate ground support performance at TGM, extensometer monitoring data from other locations in the mine should be utilised and interrogated to verify, strengthen or disprove the results in this paper. Further work may also be found using the same methodology in interrogating hanging wall overbreak data in a separate model calibration.

References

Brockman, M 2018, *Boston Shaker Underground FS Factual Geotechnical Report*.

Brockman, M 2019, *Boston Shaker Stope Cablebolting Options*.

Mills, K & Puller, J 2024, *Overcore Measurements in Boreholes BSD387 and HDD426 at Tropicana Gold Mine (Report No. TROP5637)*, SCT Operations Pty Ltd.

TGM Geology 2023, *BS3 1890 52S Final Reconciliation Sheet*.

TGM Geotechnical 2023, *TGM July 2023 Underground Monthly Report*.

TGM Geotechnical 2026, *TGM Underground Ground Control Management Plan*.

Tropicana Joint Venture 2023, *Tropicana Joint Venture*, https://www.tropicanajv.com.au/irm/content/history.aspx?RID=410

Wiles, TD 2007, 'Evidence Based Model Calibration for Reliable Predictions', in Y Potvin (ed.), *Deep Mining 2007: Proceedings of the Fourth International Seminar on Deep and High Stress Mining*, Australian Centre for Geomechanics, Perth, pp. 3–20, https://doi.org/10.36487/ACG_repo/711_Wiles